WORLD JOURNAL OF PHARMACEUTICAL RESEARCH
Coden USA: WJPRAP Impact Factor 8.63
Volume 15, Issue 9, 995-1019. Research Article ISSN 2277–7105

STRUCTURE-BASED DESIGN OF CURCUMIN ANALOGS AS POTENTIAL EGFR AND XANTHINE OXIDASE INHIBITORS: A COMPUTATIONAL APPROACH

Narsaiah Chelimela, Shobha Rani Satla*

Centre for Pharmaceutical Sciences, Jawaharlal Nehru Technological University, Hyderabad, Kukatpally, Hyderabad-500085, Telangana State, India.

Article Received on 31 March 2026,
Article Revised on 21 April 2026,
Article Published on 01 May 2026,

https://doi.org/10.5281/zenodo.19879742

***Corresponding Author**

Prof. Shobha Rani Satla

Centre for Pharmaceutical Sciences, Jawaharlal Nehru Technological University, Hyderabad, Kukatpally, Hyderabad-500085, Telangana State, India.

How to cite this Article: Narsaiah Chelimela, Shobha Rani Satla*. (2026). Structure-Based Design of Curcumin Analogs As Potential Egfr And Xanthine Oxidase Inhibitors: A Computational Approach. World Journal of Pharmaceutical Research, 15(9), 995–1019.

ABSTRACT

Therapy against cancer prevention currently revolves around the use of plant-derived anticancer drugs. In this regard, Curcumin underlines a high potential as an anticancer drug with a high affinity toward different drug targets explored in the pathophysiology of cancer. To counteract the pharmacokinetic insufficiencies of curcumin, a library of triferuloyl methane analogs were designed using computational tools. Initially, a target search was carried out for these derivatives and the most relevant ones were selected for molecular docking. Molecular docking identified hit molecules **22** and **902** against EGFR2, and **890** and **902** against Xanthine oxidase with significantly higher docking scores than co-crystallized ligands. The obtained docked complexes were subjected to MD simulations for 100s. Determination of all the relevant parameters revealed the ability of these hit molecules against these drug targets. Furthermore, MM-GBSA studies evaluated the binding free energies of the complexes, thereby corroborating the potential of the hit molecules to bind with these targets.

KEYWORDS: EGFR2, Xanthine oxidase, Molecular docking, Molecular dynamics, MM-GBSA.

1. INTRODUCTION

Recent literature says that the anticancer drug discovery is strongly associated with computational drug discovery approach than traditional drug discovery because it takes a lot of time, effort, complexity, and millions of dollars and high rate of failures of the drug candidates during clinical trials.[1] Therefore, anticancer drug discovery is much more simplified and easier to finds potent drug candidates against specific diseases like cancer by using Computer Aided Drug Design (CADD), includes techniques like molecular docking, molecular dynamics simulations, QSAR analysis. Molecular docking approach and MD simulation studies helps to know the possible binding interactions and an atomic-scale interactions between biological target and ligand respectively by using interatomic interaction model with femtosecond-level precision.[2-5] Several FDA-approved anticancer agents such as Crizotinib (lymphoma, esophageal and lung) and Axitinib (renal cell carcinoma) were developed using computational tools through structure-based design.[6]

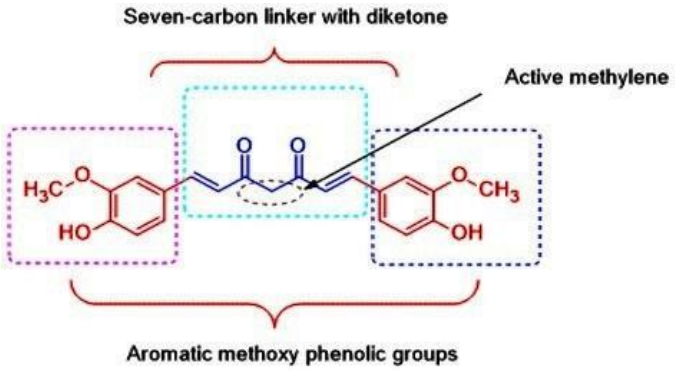

Fig. 1: Structural components of curcumin.

A plethora of natural products and their derivatives are used as an anticancer agent. Among them Diferuloylmethane (curcumin) is shown potential activity than doxorubicin, cisplatin, and 5-fluorouracil against various cancer types. Curcumin also maintains very safe profile even at higher doses (100mg/day)[7-12] (Fig. **3**). Furtherly, the scaffold of curcumin and its derivatives is more research interest due to a significant active methylene group, that serves as a connecting bridge between two ferulic acid residues and α, β-unsaturated diketone moiety, aromatic methoxy phenolic groups, and a hepta-carbon linker, play crucial roles in its biological activity[13-17] **(**Fig. **1)**. Some of the curcuminoids are available commercially as curcumin (**1**), desmethoxycurcumin (**2**), bisdemethoxycurcumin (**3**) and cyclocurcumin (**4**) (Fig. **2**). However, some complex challenges are also associated with the pharmacokinetics of curcumin and its derivatives, such as low absorption resulting from inadequate solubility,

diminished plasma concentrations, limited bioavailability, and suboptimal tissue distribution.[18-19] Design and development of such analogs with anti-cancer activity is currently a challenge for pharmaceutical research. To address these limitations of curcumin and for the cytotoxic investigation, insilico drug designing and molecular docking tools are quite helpful before synthesizing a novel derivative of curcumin.[20-21]

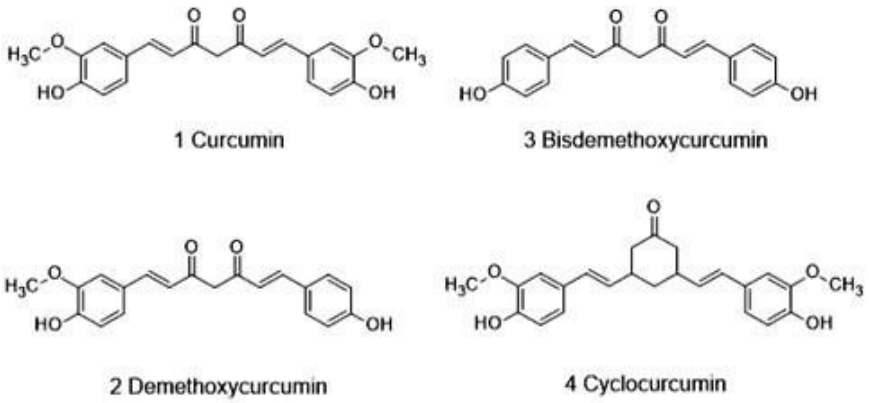

Fig. 2: Structures of Curcuminoids.

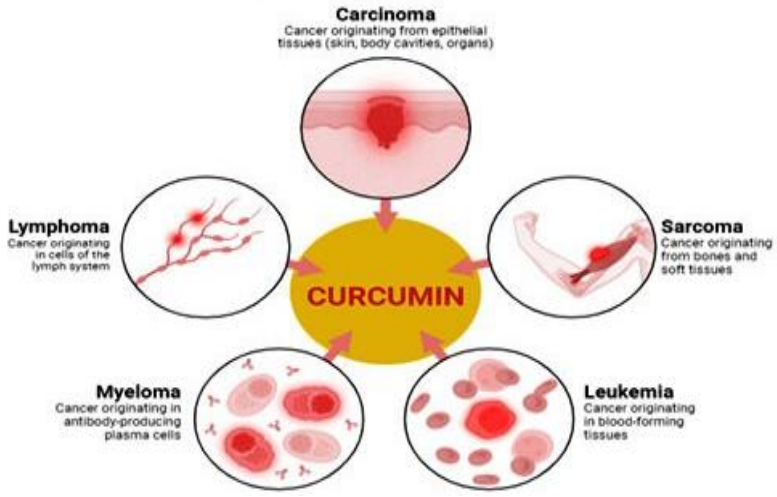

Fig. 3: Curcumin therapeutically potential to different cancers.

The substitution of an additional feruloyl moiety onto the active methylene group of diferuloyl methane, along with further substitutions at various positions on the three phenyl rings, informed by prior research findings have been improvised. We assume that the presence of another substituted feruloyl moiety in the scaffold may enhance the anticancer activity with an improved pharmacokinetic profile. In the current investigation, a library of triferuloyl methane analogs is designed using various computational tools (Fig. **4**).

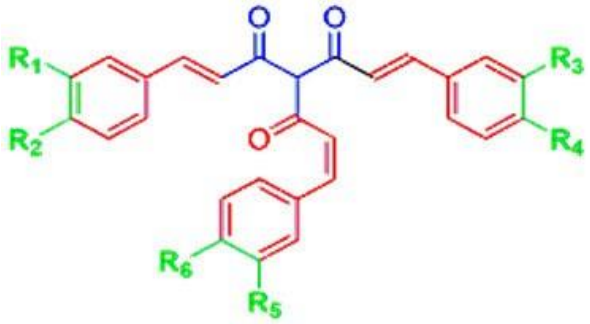

Fig. 4: Triferuloyl methane scaffold.

Despite extensive research on curcumin's anticancer potential, there is limited in silico analysis of its specific interactions with target proteins. This study addresses this gap by evaluating curcumin derivatives using molecular docking, molecular dynamics (MD) simulations, and MM-GBSA to: (1) assess binding with two target proteins, (2) analyze ligand-receptor stability, and (3) estimate binding free energy. The strength of this study is to provide a detailed evaluation of curcumin derivatives. However, this study has limitations. In silico analysis lacks experimental validation in vitro and in vivo, which are necessary to confirm the predicted bioactivity and pharmacokinetic properties.[22-24]

2. MATERIALS AND METHODS

2.1. Materials

Ligand structure drawing, 3D conversion, and initial energy minimization were performed utilizing the pcm10 tool (Serena Software, Bloomington). The Ligprep tool of Schrodinger was used for the preparation of the ligands. All protein structures were accessed from the PDB database. In the execution of Molecular docking analysis studies, the glide tool of Schrodinger was utilized. The Desmond module (D. E. Shaw Research, New York), was employed for performing the Molecular Dynamics simulations and subsequent analysis.

2.2. Designing of the Library of Triferuloyl methanes

The curcumin structure was designed into the triferuloyl methane scaffold by making another arm at the active methylene carbon atom as a unifying feature found in the curcuminoid structures as depicted in Fig. **2**. A total of 950 structures were designed involving the substitution of three phenyl rings at the ortho, para, and meta positions, along with the presence of an active methylene group as mentioned in **Table S1** of the supplementary data. All two-dimensional structures were archived as .mol files and these 2D files were then converted into three-dimensional structures. The resulting 3D structures were energy-

minimized utilizing the MMFF94 force field. The minimized structures have been saved in the protein data bank (.pdb) format.

2.3. Molecular docking analyses

The target genes/protein prediction was performed by using the bindingDB online server and Swiss Target Prediction for the representative designed molecules.[10,21] After the comparative analysis of the scores and ratio data of the two servers, potential anticancer targets like Xanthine oxidase (3nvy) and Endothelial Growth Factor Receptor (EGFR2) (3w2r) were selected as target proteins for Docking. 3D structures of selected targets were accessed from the PDB database. Using the Glide program of Maestro, a grid box of 16×16×16 Å was made around the selected binding cavity of the proteins 3nvy and 3w2r. The possible interactions and affinities of the compounds were determined using flexible docking in the Glide program. Using the Extra Precision (XP) docking tool, Molecular docking was performed keeping all the parameters set to default values.[22,23] The top 2 molecules with the best docking scores and valid amino acid interaction profiles were selected for further stages.

2.4. MD Simulations

Molecular dynamics simulations were performed by using the Desmond tool of the Schrodinger suite. The methodology used in previous research studies was adapted for this study.[24,25] This study focused on the selection of the two highest-ranking protein-ligand complexes, determined by the docking scores of the ligands **22** and **902** for EGFR2 (3w2r), as well as **902** and **890** for Xanthine oxidase (3nvy). The analysis encompassed various parameters, including the RMSD, RMSF, Ligand properties, and interaction profiles.

2.5 MM-GBSA studies

MM-GBSA studies were performed using the Prime module of the Schrodinger suite. Trajectory files were loaded onto the software in the. trj format obtained after MD simulation. Later, the complex was extracted for every 5ns starting from 0ns up until 100ns. Later, each complex obtained was separated into separate ligand and protein structures. Each of these structures was then calculated for their binding free energy at that particular time point. Later, all the calculations and plotting of the graph with $\Delta G_{\text{Binding energy}}$ in kcal/mol on the Y-axis vs Time in ns on the X-axis were performed using the MS-Excel program from MS Office 2021.[26]

3. RESULTS AND DISCUSSION

3.1. Molecular Docking

The potential macromolecular targets for the triferuloyl methane compounds were identified utilizing the BindingDB and Swiss Target Prediction tool. A range of proteins implicated in cancer pathophysiology, such as Xanthine oxidase (3nvy) and Endothelial Growth Factor Receptor 2 (3w2r), in addition to other recognized target proteins, were examined. Predictions indicate that Triferuloyl methane analogs may effectively inhibit 3nvy and 3r2r specifically, with a likelihood exceeding 0.7. Further analysis indicated that enzymes are likely target proteins for diverse pharmacological activities, as revealed through literature mining and their activity profiles.

The compounds analyzed demonstrated an XP G-score maximum of -12.367 kcal/mol against Xanthine oxidase (3nvy), and -14.277 kcal/mol against Endothelial Growth Factor Receptor 2 (3w2r). The potential affinity of these compounds was validated by examining the binding cavities of the target proteins. To validate the docking methodology, a docking simulation was conducted comparing the drawn structure of the co-crystallized ligand with its conformation within the protein. It was observed that certain triferuloyl methane derivatives exhibited G-scores exceeding that of the native ligand, which were recorded at -12.367 and -14.227 kcal/mol for the same enzyme (Table **1**).

Table 1: Docking interactions of top 2 ligands for 3w2r and 3nvy.

Compound	Glide score	Hydrogen bonding with amino acid residues (atomic distance in Å)	Other interactions
3w2r			
22	-14.277	Met793 (2.53 Å and 2.10 Å), Asp800 (1.69 Å and 1.57 Å), Asn842 (1.88 Å), and Asp855 (1.90 Å).	--
902	-12.054	Leu788 (1.71 Å), Cys797 (2.11 Å), Asp800 (1.86 Å, and 1.91 Å), Asp837 (1.72 Å), Asn842 (2.12 Å), and Asp855 (1.70 Å)	π-cation: Arg841 (6.38 Å)
3nvy			
902	-12.367	Leu648 (1.85 Å), Asn768 (1.97 Å), Thr1010 (1.78 Å), and Asn1073 (2.01 Å)	π-stacking: Phe914 (3.73 Å), Phe1009 (4.72 Å), Phe1013 (5.35 Å and 4.69 Å) Salt bridge: Arg880 (3.30 Å)
890	-12.298	Asn768 (2.10 Å) and Thr1010 (1.97 Å)	π-stacking: Phe1009 (5.11 Å), Phe1013

			(4.82 Å). Salt bridge: Arg880 (2.60 Å)

3.1.2 Glide scores and binding interactions with EGFR2

Molecular modeling experiments have revealed the importance of amino acid residues like Lys745, Leu 788, Ile 789, Met790, and Met793 which are crucially involved in the ATP site of the enzyme. It is composed of a hydrophobic binding pocket with Leu 747, Ile 759, Met 766 Leu 777, and Leu 788. Additionally, another structural element, the DFG motif is composed of Asp855, Phe856, and Gly857.[27,28] The urea moiety of the Co-crystallized ligand showed hydrogen-bonding interactions with Ala722 and Asp837. The pyrrolo-pyrimidine part of the structure formed hydrogen bonds with Asp855 and Phe856. A π-cation interaction was observed with Arg841. It showed an XP-G score of -7.764. The library of compounds showed XP-G scores in the range of 4.096 to -14.277. Overall, 51 ligands showed XP G-scores higher than or equal to -10. The best score of -14.277 throughout the series of compounds displayed by **22**, which bore a hydroxyl substitution. It was found to undergo hydrogen-bonding interactions with Met 793 (2.53 Å, and 2.10 Å), Asp 800 (1.69 Å, and 1.57 Å), Asn 842 (1.88 Å), and Asp 855 (1.90 Å). The next best was **902** which bore a hydroxylamine and hydroxyl substitution. It revealed a docking score of -12.054, against EGFR2. It was found to interact with Leu 788 (1.71 Å), Asp 800 (1.86 Å and 1.91 Å), Asp 837 (1.72 Å), Asn 842 (2.12 Å), and Asp 855 (1.70 Å) by hydrogen-bonding interactions and Arg 841 (6.38 Å) by π-cation interaction (Fig. **5**).

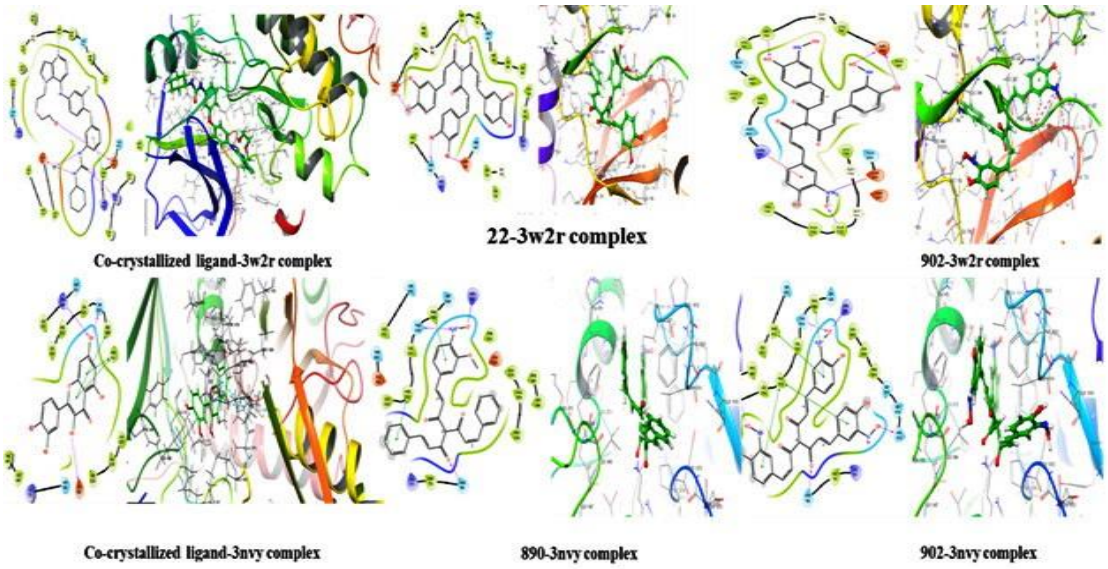

Fig. 5: 2D and 3D bonding amino acid interactions of co-crystallized ligands and hit molecules against target proteins.

3.1.3 Glide scores and binding interactions with Xanthine Oxidase

Xanthine oxidase is structurally composed of two domains- an α-β roll and an α-orthogonal bundle. It bears two substrate-binding sites namely, the Molybdenum-molybdopterin site (Mo-Pt site) that catalyzes the oxidation of xanthine, and the Flavin adenine dinucleotide site which is responsible for generating superoxide anion. Inhibition at the Mo-Pt site is thus, key to the inhibition of xanthine oxidase activity. Previous modeling experiments have vividly indicated the importance of key amino acid residues in the Mo-Pt site like Leu648, Asn768, Glu802, Leu873, Arg880, Phe914, Phe1009, Thr1010, Val1011, and Glu1216. It was noted that for the oxidation reaction, Glu1261 acts as a nucleophile, Phe904, and Phe1009 surround the substrate, and Gln767 binds with the molybdoprotein. Additionally, Arg880 is hydrogen-bonded to the distal end of the substrate. Some of these residues also form a small channel that accesses the Molybdenum.[29-31] The co-crystallized ligand, Quercetin occupied the Mo-Pt site and showed hydrogen-bonding interactions with amino acid residues Glu802, Ser876, Arg880, and Thr1010. This was due to free hydroxy groups in the structure. It exhibited an XP-G score of -8.380. The library of docked ligands revealed a docking score in the range of 5.817 to -12.367. As many as 76 ligands showed XP G-scores higher than or equal to -10. **902** bore a hydroxylamine and hydroxyl substitution revealed a docking score of -12.367 against 3nvy. It was found to form hydrogen bonds with Leu 648 (1.85 Å), Asn 768 (1.97 Å), Asp 1073 (2.01 Å), and Thr 1010 (1.78 Å). Phe 914 (3.73 Å), Phe 1009 (4.72 Å), and Phe 1013 (5.35 Å, and 4.69 Å) by π-π stacking interactions and the salt bridge interactions were formed with Arg 880 (3.30 Å) (Fig. **5**). **890** bore one hydroxylamine substitution. It showed a docking score of -12.028, against 3nvy, and displayed hydrogen bonds with Asn 768 (2.10 Å) and Thr 1010 (1.97 Å). Phe 1009 (5.11 Å) and Phe 1013 (4.82 Å) were involved in π-π stacking interactions, and the salt bridge interaction was formed with Arg 880 (2.60 Å) (Fig. **5**). The hit ligands seemed to bear potential to act as a competitive antagonist competing with molybdoprotein for the Mo-Pt site.

3.2 MD Simulations Analysis

Molecular dynamics simulations serve as an in-silico technique to evaluate the stability of the protein-ligand complex. It provides insights into the binding affinity of the ligand to its associated protein, which is affected by both intra- and intermolecular forces. Analyzing a range of parameters is vital for achieving a clear understanding of the conformational stability of protein-ligand complexes. Metrics such as RMSD, RMSF, secondary structural features, amino acid interaction profiles, ligand properties, and trajectory snapshots reveal a complete

understanding of the ligand-protein complex stability. Hit molecules **22** and **902** were selected for protein 3w2r, while compounds **902** and **890** were chosen for protein 3nvy. In addition, the wild-type proteins (absence of any ligand in its binding site) were also subjected to 100ns simulations. These wild-type proteins served as reference structures for the analysis.

RMSD functions as a measure of the change in the structural features of the protein-ligand complex in comparison to the amino acid residues present in the protein. An exemplary graph of RMSD would present a uniform profile, demonstrating the stability of the complex. In contrast, continuous changes observed in the graph might suggest a level of flexibility within the structure, thereby implying potential instability. Correlation between the graphs of protein and protein-ligand complex indicates whether the ligand and protein have adjusted their structures to make for a better fit. Herein, the wild-type protein 3w2r demonstrated significant stability throughout the analysis, with an average RMSD of about 3 Å. It was noted that wild 3w2r protein showed higher levels of flexibility till 40ns but thereafter, the RMSD graph was maintained at a plateau phase till the end of runtime. The ligand-protein complex with ligand **22** had an average RMSD value of about 1.3 Å for the complex, whereas the protein Cα atoms showed an average RMSD of about 2.4 Å. The RMSD values were significantly low throughout the run time, suggestive of the high stability of the protein-ligand complex. Whereas, the average RMSD value of ligand **902** in complex with protein was about 1.6 Å, and that of Cα atoms was about 2.8 Å. Even though the averages were slightly higher than ligand **22**, still, there was high stability of the complex. Both the ligands showed a plateau phase throughout the RMSD graphs. The RMSD graph of 3nvy was maintained at low RMSD values throughout the timeline with minimal flexibilities in the amino acid residues. It showed an average RMSD value of about 2.2 Å throughout the run time. Ligand **902** in complex with protein showed an average RMSD value of about 5 Å and for Cα atoms was about 1.75 Å. Ligand **902** showed significant fluctuations in the complex up until 35ns after which it showed a plateau phase till 70ns. Post 70ns, there was still some fluctuation till 90ns after which it revived the plateau phase. Ligand **890** showed an average RMSD value of about 6 Å. Whereas, the Cα atoms showed an average RMSD value of 2.1 Å. The reasons for these fluctuations would be due to slight changes in the ligand conformation to fit better in the binding pocket. It may also be that some structural changes are occurring in the protein conformation and thus, subsequent changes in the ligand conformation to accommodate that change (Fig. **6**).

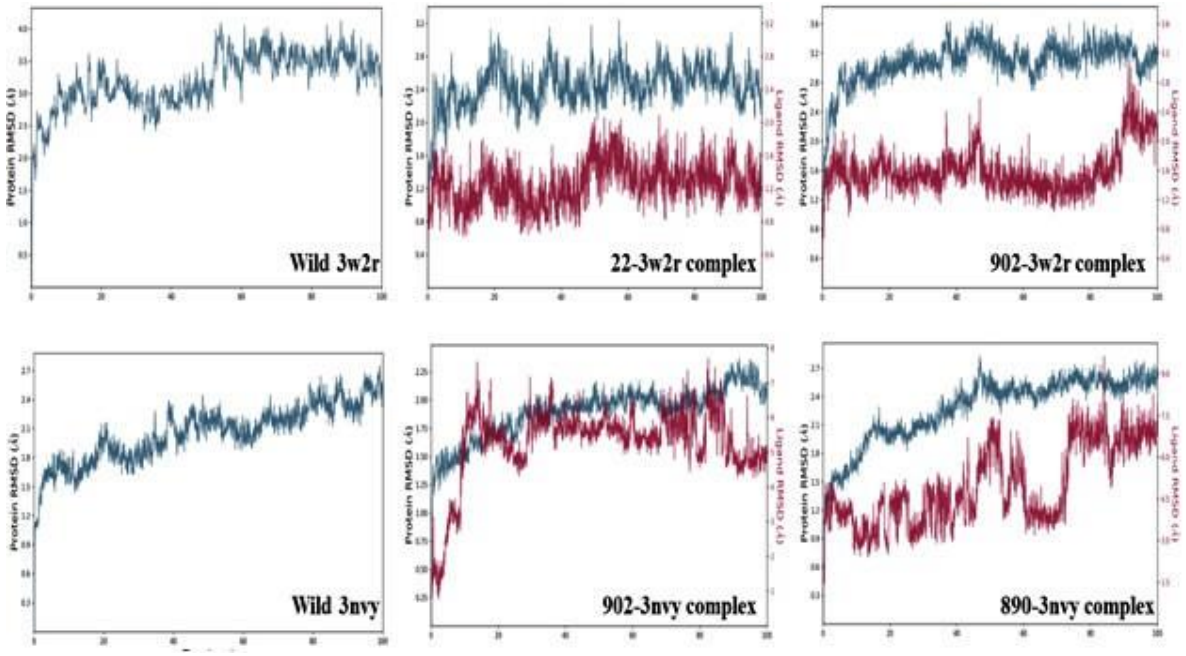

Fig. 6: RMSD graphs of wild protein targets and their complexes with hit molecules.

An evaluation of the structural stability of amino acid residues in the protein backbone was performed through the application of the RMSF tool. This examination reveals important information regarding the flexible regions of the protein and the characteristics of the amino acid residues that engage in different bond formations with the ligand. It is common for amino acid residues that take part in bond formations to exhibit low RMSF values. These values are representative of a favorable RMSF graph, highlighting the rigidity associated with these residues. Similarly, the adaptability of the molecular ligands throughout the simulation was assessed using RMSF graphs. In the proteins 3w2r, the RMSF values for all amino acids were found to be between 0.5 Å to 6 Å. The highest fluctuations were shown by amino acid residues Ala698, Pro699, Ala722, The751, Ser995, and Asn996 with RMSF values above 4 Å. The average RMSF value for the protein-ligand complex of **22** was revealed to be at an average of 2.218 Å. Amino acid residues Ala698, Pro699, and Asn700 were fluctuating above 5 Å. However, all other amino acid residues showed fluctuations below 4 Å. The average RMSF of the protein-ligand complex for **902** was found to be 0.724 Å. Ala698, Pro699, Asn700, Asp984, and Glu985 showed fluctuations above 4 Å. However, none of these residues were involved in bonding interactions, hence, it did not affect the complex stability. Whereas, for 3nvy, the observed RMSF was in the range of 0.5 Å to 10 Å. Certain amino acid residues Phe196, Asn197, Asn1324, Cys1325, and Lys1326 all showed 4.5 Å. For the ligand **890** in complex with the protein, it showed an average value of 2.236 Å. It showed fluctuating residues Leu195, Phe196, Asn197, Pro198, Thr1290, Lys1291, Asn1324,

Cys1325, and Lys1326 all showed 4.5 Å. Ligand **902** in complex with protein revealed an average RMSF value of 2.124 Å. The fluctuating residues included Leu195, Lys526, Leu527, Gly528, Asp571, Thr572, Val573, Gly574, Cys1325, and Lys1326 showed RMSF values above 4 Å (Fig. **7**).

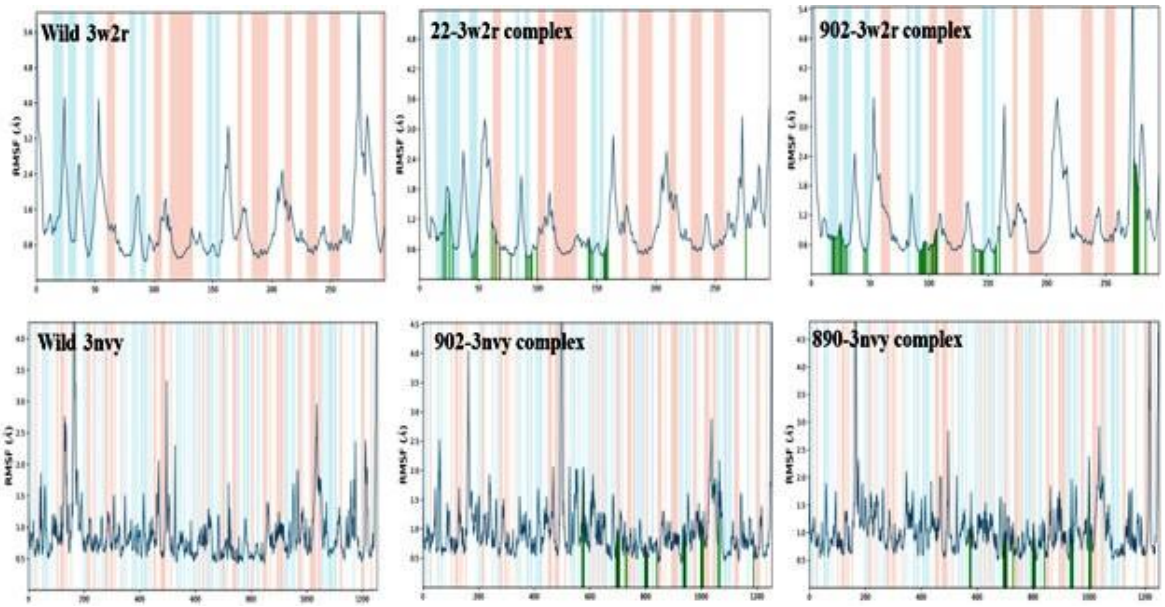

Fig. 7: RMSF graphs of wild protein targets and their complexes with hit molecules.

The analysis of significant changes in the secondary structure of a protein at both ligand-bound and unbound sites was performed using the Secondary Structural Elements (SSE) graph, which includes protein helices and sheets. More stable protein-ligand complexes exhibit a higher percentage of secondary structures. The wild-type protein 3w2r showed 28.98% α-helix and 14.72% β-strand, leading to a cumulative secondary structure percentage of 43.70%. The protein-ligand complex of **22** showed the protein's secondary structure to preserve its native features, with α-helix (29.74%), β-sheet (15.27%), and total SSE percentage (45.00%) showing remarkable similarity. The secondary structure analysis of the protein-ligand complex of **902** demonstrated that the proportions of α-helix (25.37%) and β-sheet (14.07%) formations, overall, 39.44% were comparable to those observed in the wild-type 3w2r. It can be noted that both ligands did not significantly alter the secondary structural elements of the protein significantly, thus showing good potential to be lead molecules. In comparison, the wild-type protein 3nvy revealed 23.78% α-helix and 20.65% β-strand, resulting in a total secondary structure percentage of 44.43%. (Fig. **8**).

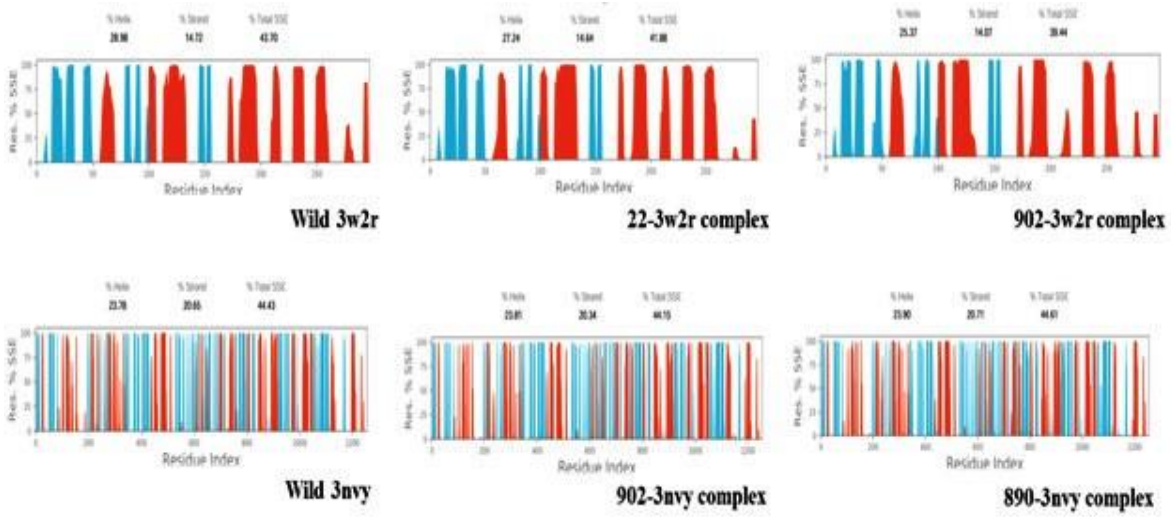

Fig. 8: Secondary structural elements' graphs of wild protein targets and their complexes with hit molecules.

The binding interactions, including their characteristics and the duration of these interactions during the simulation, were assessed through the analysis of 2D interaction diagrams that illustrated the ligands' interactions with the amino acid residues of the protein. The interaction fraction graphs of the amino acid residues were scrutinized to determine their roles in the bonding interactions. In addition, the protein-ligand interactions throughout the simulation were explored to evaluate the reliability of the contributions made by the amino acid residues to these bonding interactions. Ligand **22** in complex with 3w2r effectively established water bridges with the residues Ala722, Lys745, Met793, Asp800, Arg841, Thr854, Asp855, and Asn996, maintaining this interaction consistently throughout the simulation. Furthermore, nine hydrogen bonds were detected with the amino acid residues Ala743, Lys745, Leu788, Cys797, Asp800, Arg841, Thr854, Asp855, and Asn996. The residues Phe723, Val726, Lys745, Met790, Arg841, Leu844, and Phe997 played a significant role in hydrophobic interactions. The simulation timeline revealed consistent protein-ligand interactions involving residues Val726, Ala743, Lys745, Met790, Met793, Cys797, Asp800, Asp855, and Phe997. An average of approximately 17 protein-ligand contacts was established throughout the runtime. Similarly, **902** in complex with 3w2r revealed a total of sixteen hydrogen bonds were identified with Ser720, Ala722, Phe723, Lys745, Gln791, Met793, Phe795, Cys797, Asp800, Asp837, Asn842, Asp855, Arg858, Ser995, Asn996 and Phe997. Water bridge interactions were predominantly observed with the residues Leu718, Ser720, Ala722, Phe723, Gly7244, Lys745, Met793, Pro794, Phe795, Cys797, Asp800, Glu804, Arg841, Asn842, Asp855, Arg858, Ser995, Asn996 and Phe997. Hydrophobic interactions were noted

with Leu718, Phe723, Val726, Ala743, Met790, Leu792, Leu844 and Phe997. Additionally, ionic interactions were detected involving Lys745, Asp837, Asp855, and Arg858, with Arg858 being the primary contributor to ionic bonding. The analysis revealed that consistent protein-ligand interactions occurred with residues Ala722, Phe723, Ala743, Lys745, Met793, Cys797, Asp800, Asp837, Arg841, Leu844, Asp855, and Arg858 throughout the observed timeline. An average of approximately 20 protein-ligand contacts was established during the runtime. Furthermore, the conserved residues Lys728 and Val843 were found to engage in hydrophobic interactions with ligand **902**. A significant water bridge interaction was established between compound **902** and the water molecule Asp837, indicating a potential role in the competitive inhibition of the protein and modulation of the catalytic activity of the aspartic protease, similar to 3w2r.

The investigation of the protein-ligand interactions of the complex with **902** with the protein 3nvy revealed a total of fourteen hydrogen bonding interactions with specific amino acid residues, including Asn768, Lys771, Arg871, Asp872, His875, Ser876, Glu879, Arg880, Thr1010, Phe1013, Gln1016, Asn1073, Ser1074, and Ser1075. In addition, residues such as Leu648, Phe649, Met770, Lys771, Leu873, Phe914, Phe1009, Val1011, Phe1013, and Leu1014 were recognized for their role in hydrophobic interactions. Significant water bridge interactions were facilitated by Gly647, Leu648, Asn650, Asn768, Met770, Lys771, Ser774, Lys778, Glu802, Arg871, Asp872, His875, Ser876, Glu879, Arg880, Thr1010, Phe1013, Gln1016, Asn1073, Ser1074, Ser1075, and Glu1261. Notably, two ionic interactions were identified between Glu879 and Arg880. Throughout the study, Gly771, Ser876, and Glu879 consistently engaged in protein-ligand interactions. On average, approximately fourteen contacts between the protein and ligand were observed during the runtime. Whereas, with the protein-ligand complex of **890**, a total of thirty-three bonding interactions were identified, including six hydrogen bonds with the amino acids Asn768, Met771, Ser876, Arg880, Thr1010, and Val1011. The interactions involving water bridges were primarily attributed to the residues Gly647, Leu648, Lys771, Ser774, Lys778, Asp872, His875, Ser876, Glu879, Arg880, Thr1010, Val1011, and Phe1013. In terms of hydrophobic interactions, the key residues identified included Leu648, Phe649, Met770, Phe775, Lys778, Leu873, Phe914, Phe1009, Val1011, Phe1013, Leu1014, Pro1076, Ala1078, and Ala1079. Additionally, two ionic bonds were detected between Glu879 and Arg880. Throughout the analysis, stable protein-ligand interactions were observed with Lys771, Ser876, and Glu879. On average, approximately 10 contacts between the protein and ligand were established during the

runtime (Fig **9-11**).

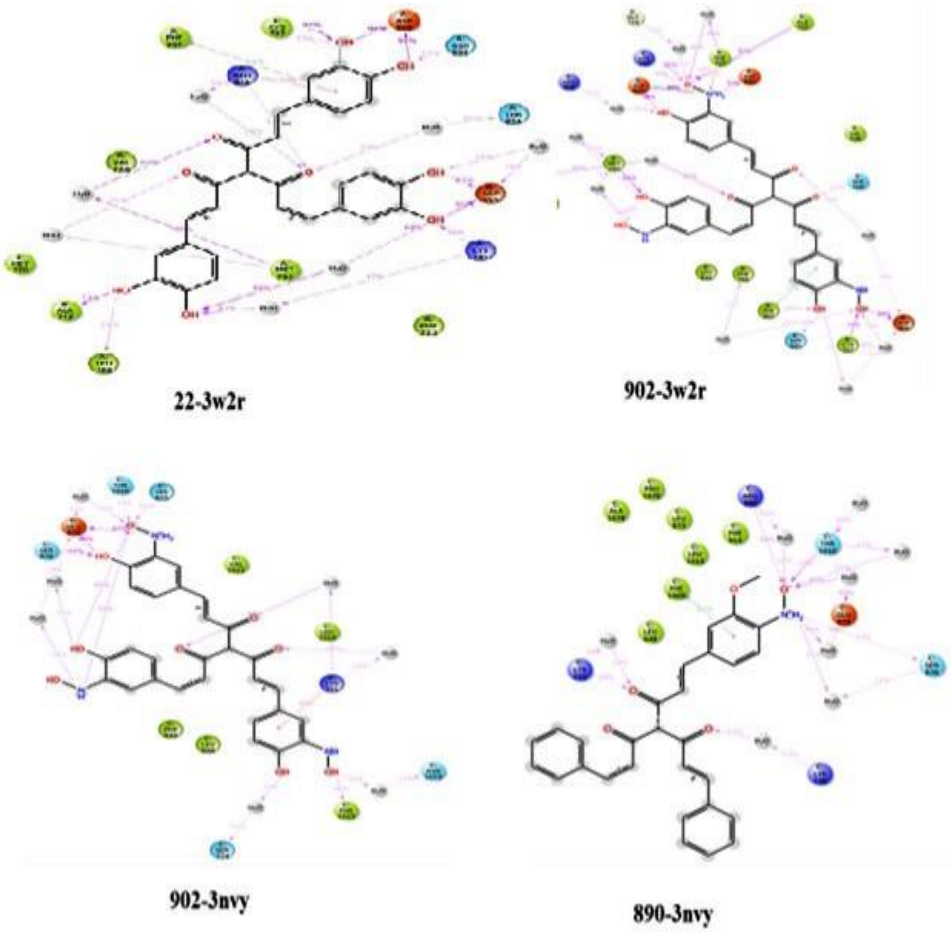

Fig. 9: 2D interaction images of hit molecules with amino acid residues of target proteins.

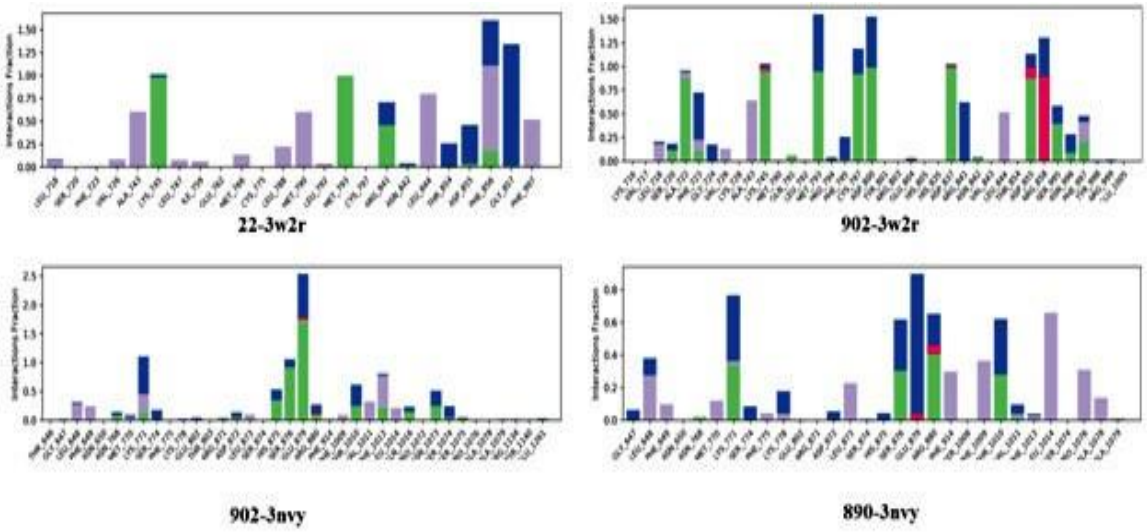

Fig. 10: Interaction fractions histogram for hit molecules in complex with target proteins.

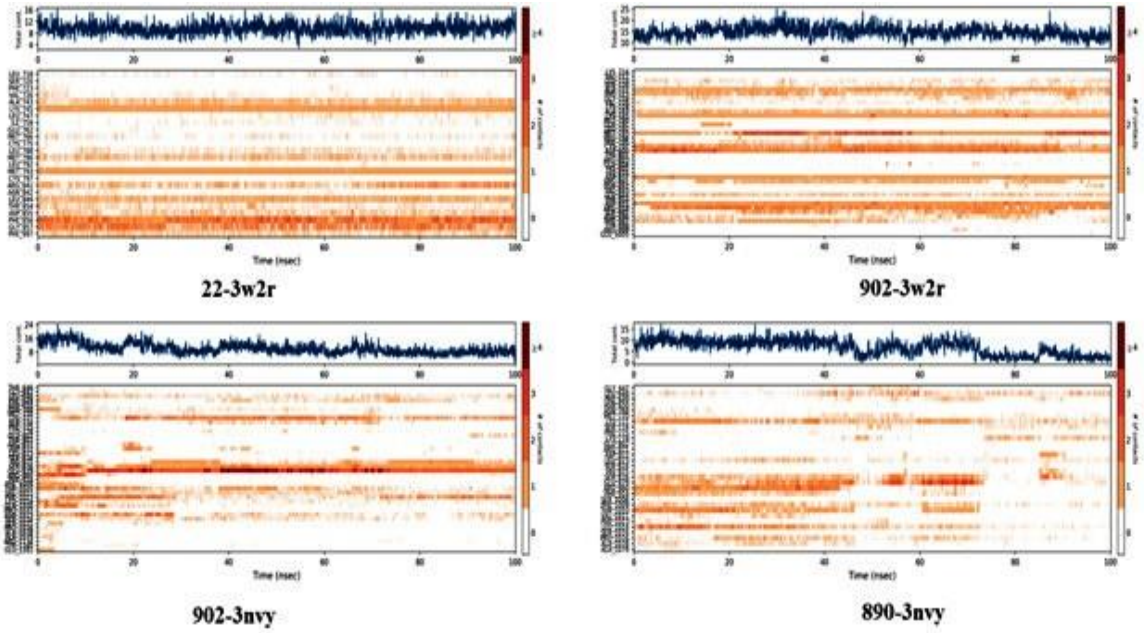

Fig. 11: Amino acid contributions and maximum number of protein contacts for hit molecules in complex with target proteins.

The ligand properties cover the average rGyr, the average SASA, PSA, MolSA, and the presence or lack of intramolecular hydrogen bonding. The rGyr serves as a crucial indicator of ligand rigidity, with a smaller value denoting a more compact complex, thus indicating greater stability. The SASA illustrates the fraction of the complex that is available for solvation. An elevated SASA value may indicate a more open conformation of the complex, which could suggest instability. In the case of ligand **22** in complex with 3w2r, the average rGyr was calculated to be about 6.5 Å, while the MolSA measured about 516 sq Å. Additionally, the SASA was found to be about 75 sq Å, and the PSA was recorded at about 150 sq Å. Some intramolecular bonding was observed with the complex throughout the timeline, but it did not affect the protein-ligand complex stability. The protein-ligand complex of **902** revealed a rGyr of about 5.55 Å, MolSA of about 475 sq Å, SASA of about 140 sq Å, and PSA of about 420 sq Å. Additionally, persistent intramolecular hydrogen bonds were identified within ligand **902**, likely resulting from the presence of hydroxyl and hydroxylamine groups at the meta and para positions on the scaffold. This interaction did not significantly influence the stability of the protein-ligand complex throughout the simulation.

For the ligand **902** in complex with 3nvy, the average rGyr was calculated to be about 6.5 Å, accompanied by MolSA of about 470 sq Å, a SASA of about 300 sq Å, and a PSA of about 420 sq Å. Additionally, some intramolecular hydrogen bonding was identified within the

ligand, formed by the hydroxyl and amine groups interacting with one of the carbonyl oxygen atoms, but it did not affect the stability of the complex significantly. Ligand **890** in complex with 3nvy, revealed a rGyr at about 5.2 Å, with a MolSA of about 450 sq Å. The SASA was measured at about 270 sq Å, while the PSA was recorded at about 165 sq Å. No intramolecular hydrogen bonds were identified within the ligand (Fig. **12**).

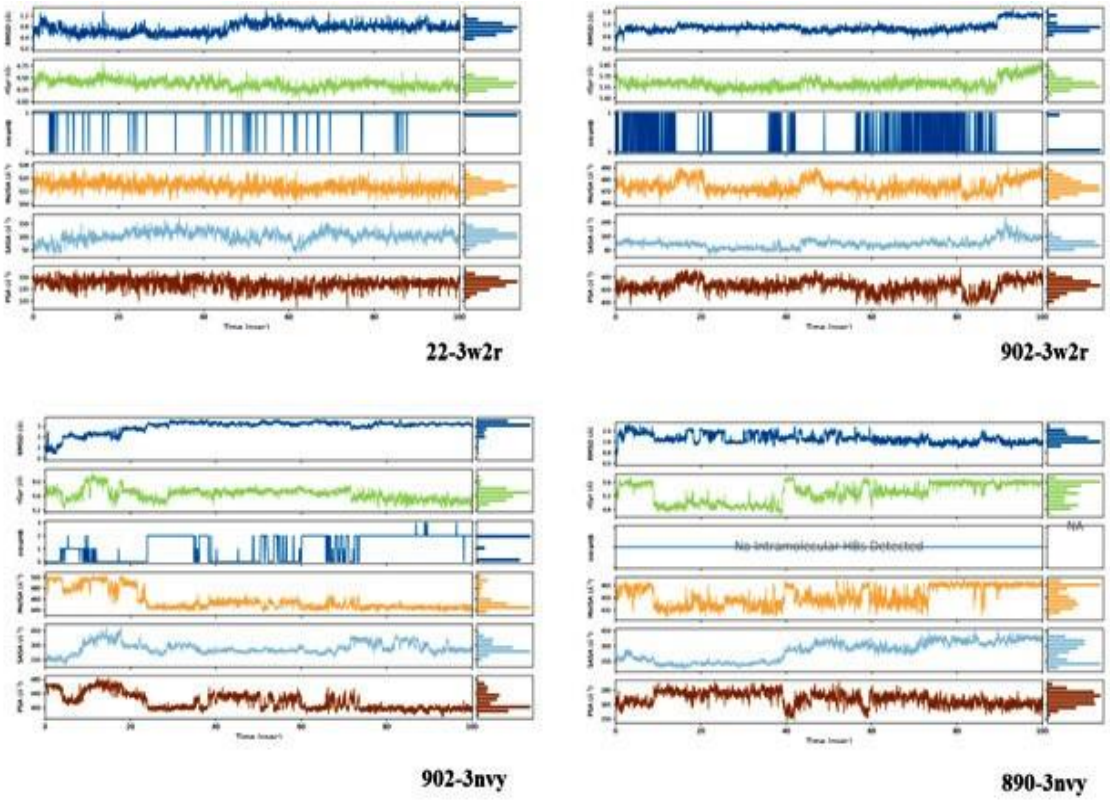

Fig. 12: Ligand properties of hit molecules in complex with target proteins.

The possible conformations of the wild-type proteins 3w2r and 3nvy were analyzed in trajectory images. These conformations are essential for assessing the stability of the protein during the simulation duration. The trajectory images of the complexes were reviewed at multiple time intervals during the simulation to identify any changes in the binding conformations of the ligands after stability was reached. Wild 3w2r and 3nvy revealed very minor flexibilities throughout the run time of 100ns depicting its stable structural alignment (Fig. **13-14**). Ligand **22** in complex with 3w2r showed a high amount of conformational stability as revealed through trajectory images. It revealed minor fluctuations throughout 100ns (Fig. **15**). Trajectory images also revealed the stability of **902** in complex with 3w2r stationed firmly in its binding pocket with minimal flexibilities throughout the 100ns timeframe (Fig. **16**). The complex of ligand **902** with 3nvy revealed that the ligand

maintained a Y-shaped conformation in the binding pocket of the enzyme with slight flexibility throughout the timeline as corroborated by trajectory snapshots (Fig. **17**). Ligand **890** showed a compact conformation till 30ns after which it was revealed to have a Y-shaped conformation which was more relaxed and afforded better accommodation in the binding site for compound **890** (Fig. **18**).

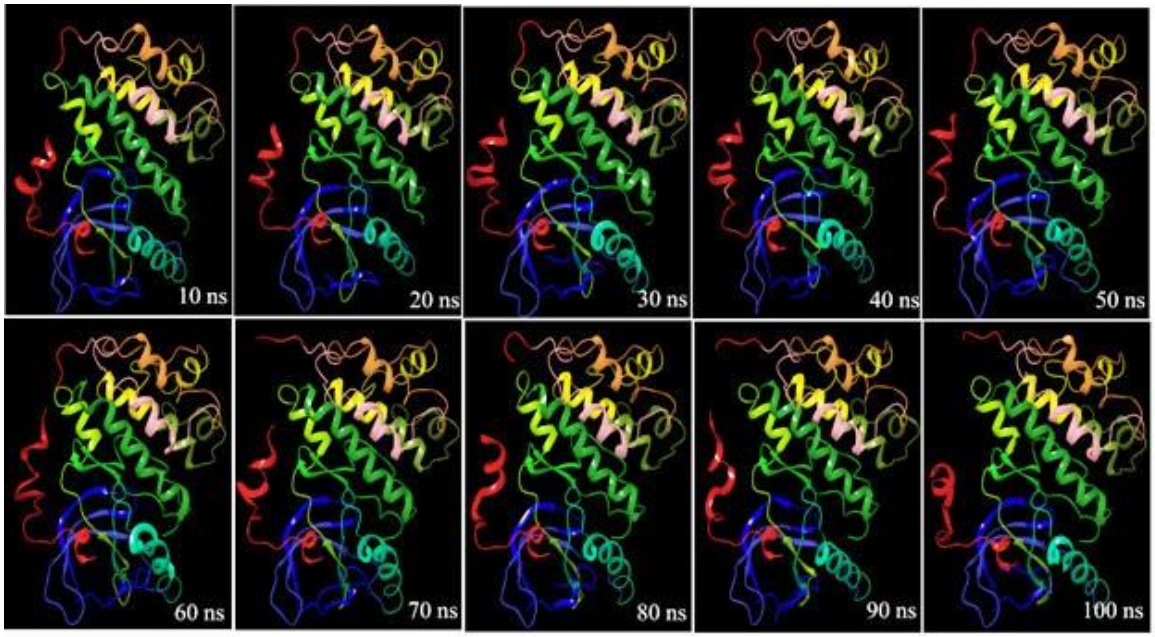

Fig. 13: Trajectory images of wild 3w2r over 100ns timeline.

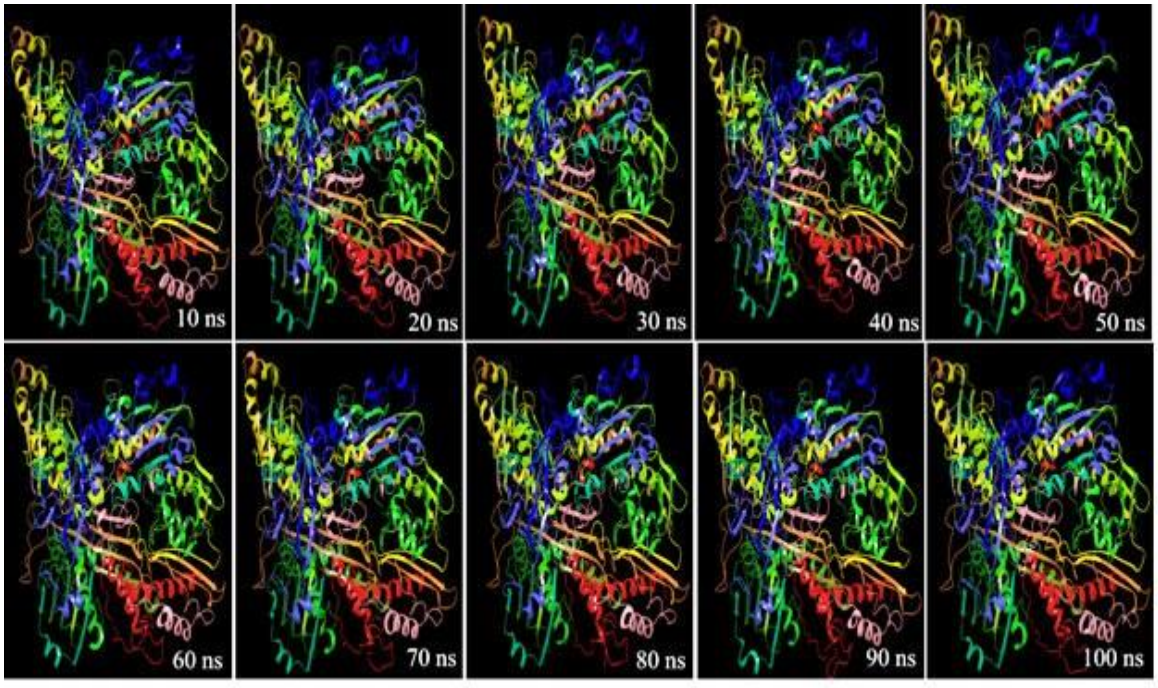

Fig. 14: Trajectory images of wild 3nvy over 100ns timeline.

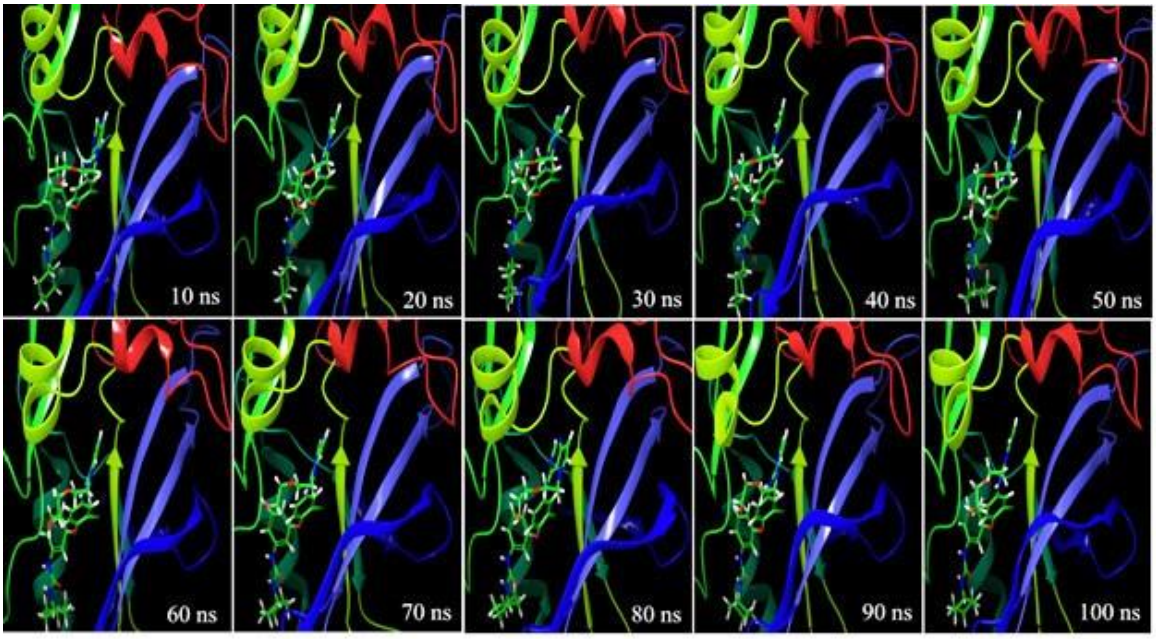

Fig. 15: Trajectory images of Compound 22 in complex with 3w2r.

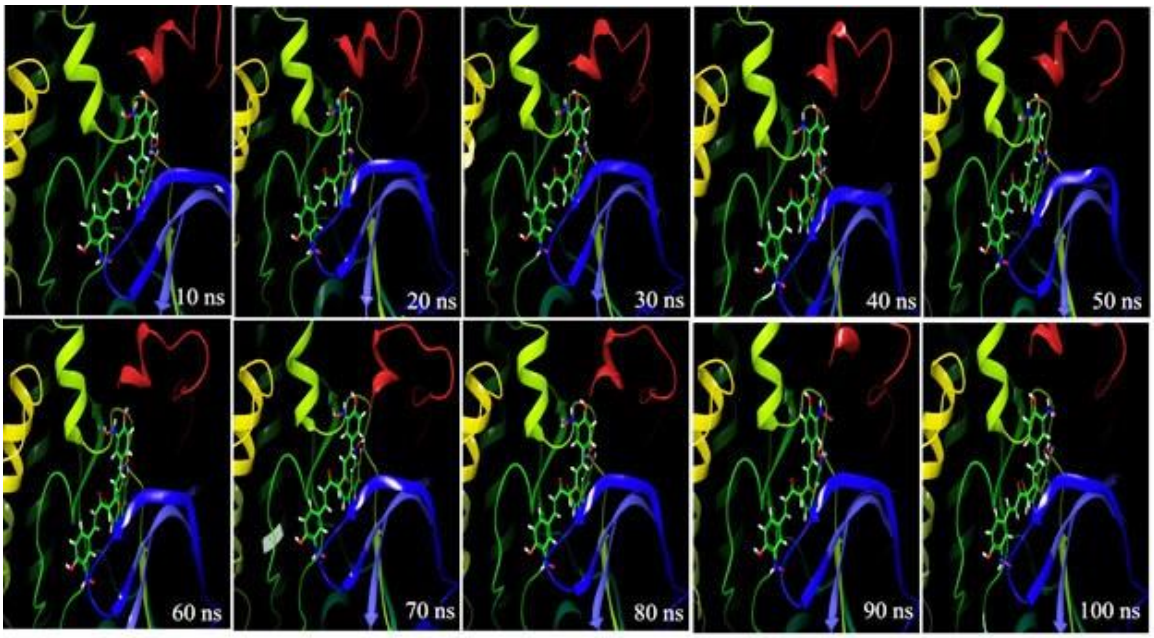

Fig. 16: Trajectory images of Compound 902 in complex with 3w2r.

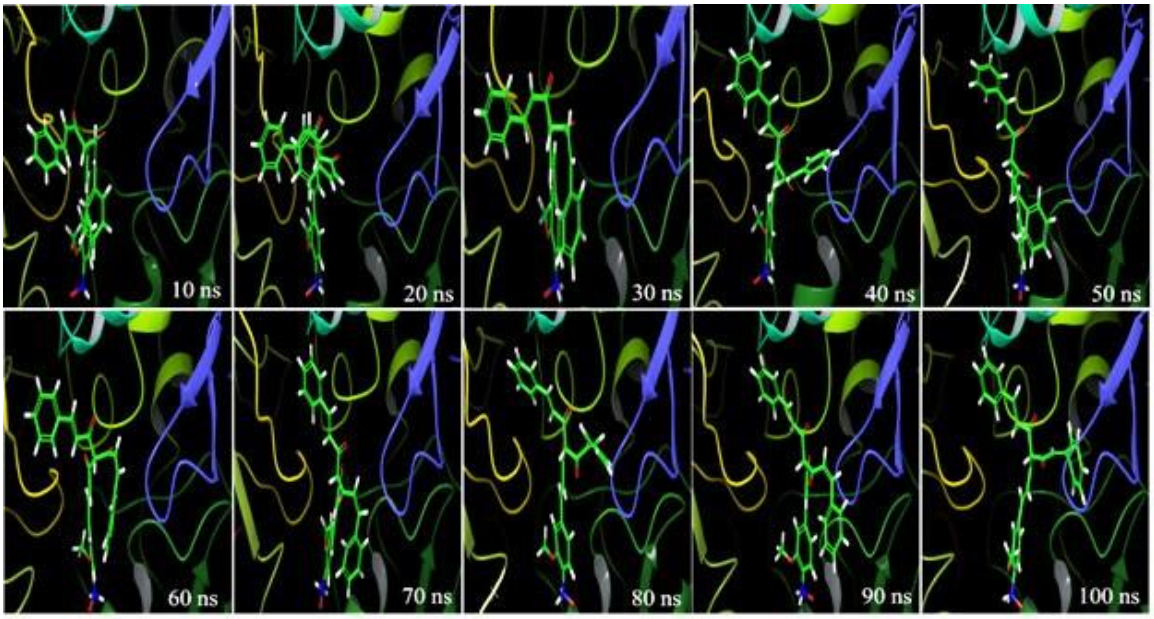

Fig. 17: Trajectory images of Compound 902 in complex with 3nvy.

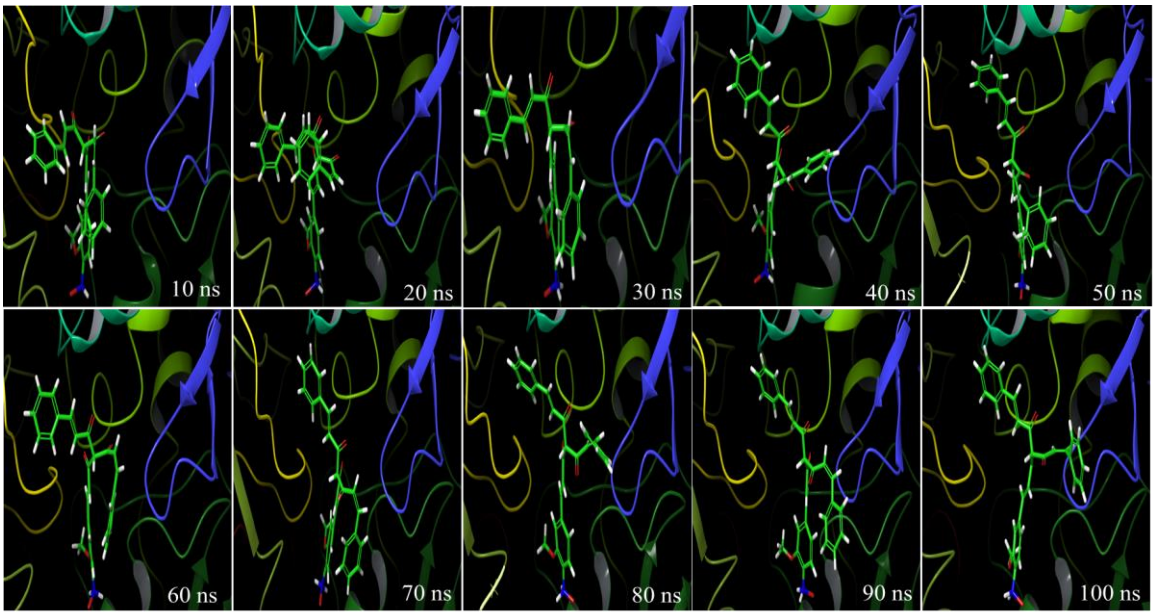

Fig. 18: Trajectory images of Compound 890 in complex with 3nvy.

3.3 MM-GBSA calculations and analysis

Changes in binding free energy of the complex ($\Delta G_{\text{Binding energy}}$) over 100ns were assessed by MM-GBSA studies. The final energy calculation was a result of multiple energy parameters including Columb energy owing to charge interactions, Van Der Waals interactions, Lipophilic interactions, and Hydrogen bonding energy. Ligand **22** in complex with 3w2r revealed a significantly low value of binding free energy as -138.987±19.71 kcal/mol. The highest contribution to the binding free energy was owing to the Lipophilicity and Van Der

Waals interactions (Table **2-3**). The graph of change in binding free energy vs time revealed the lowest energy at -155.69 kcal/mol and the highest energy value at -126.14 kcal/mol. The ligand revealed very stable and low binding free energy throughout the run time, thus corroborating the high stability of the complex (Fig. **19**). Ligand **902** in complex with 3w2r revealed a binding free energy value of -97.612±11.74 with the highest contribution due to Van Der Waals and Lipophilic interactions as observed with the previously described complex (Table **2-3**). The lowest point in the graph was -109.36 kcal/mol which altered to a maximum point of -78.35 kcal/mol. The binding free energy was relatively maintained throughout the run time however, it was lesser than that observed with ligand **22** (Fig. **19**). Similarly, with ligand **902** in complex with 3nvy, it was observed that the binding free energy was -72.583±13.58 kcal/mol. The highest contribution corresponded to Van Der Waals interactions and Lipophilic interactions (Table **2-3**). The graph of ligand **902** in complex in 3nvy over 100ns was found to be at maximum owing to the value -45.07 kcal/mol, while the minimum was observed at -106.17 kcal/mol. The ligand underwent several small structural changes throughout the run time but showcased an overall stable graph (Fig. **19**). For the ligand 890 in complex with 3nvy, it was observed that the overall binding free energy was -71.052±14.71 kcal/mol with major contributions from Van Der Waals interactions and Lipophilic interactions (Table **2-3**). The graph depicting the change in binding free energy over time revealed the lowest value at -102.69 kcal/mol and the highest value at -49.19 kcal/mol. However, despite persistent changes in the binding free energy over run time, overall, the graph was maintained stable.

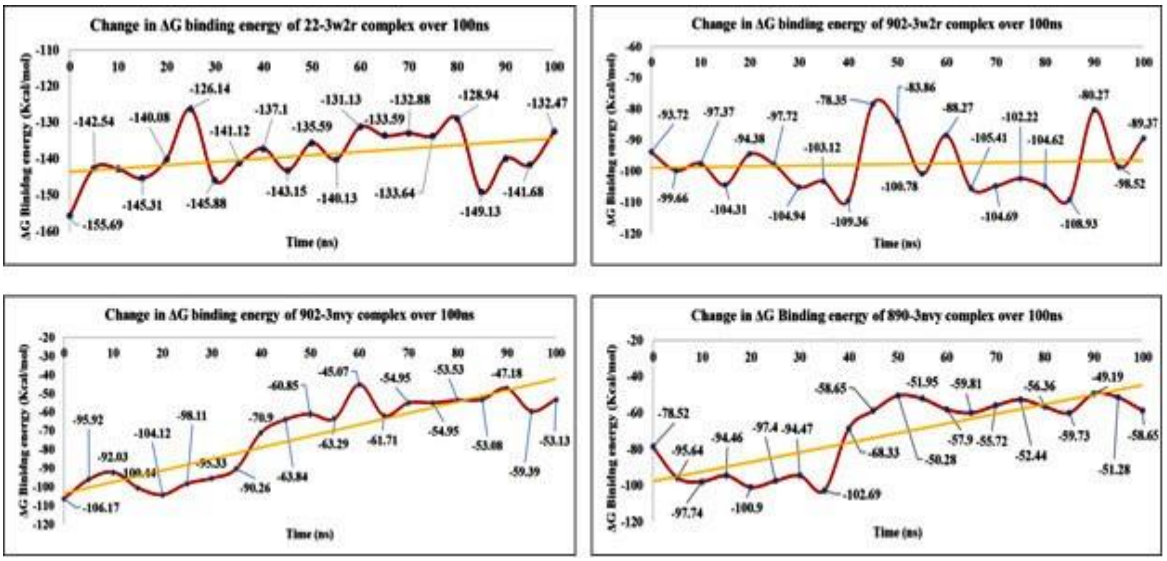

Fig. 19: MM-GBSA graphs depicting the change in the binding energy of the hit molecules in complex with wild protein targets over 100ns.

Table 2: Average $\Delta G_{binding}$ energy for ligands throughout 100ns.

Ligands	Average $\Delta G_{binding}$ energy (Kcal/mol)
3w2r	
22	-138.987
902	-97.612
3nvy	
902	-72.583
890	-71.052

Table 3: MM-GBSA interaction energies of Ligand complexes (100ns).

Ligands	$\Delta G_{binding}$ Energy	$\Delta G_{binding}$ Coloumb	$\Delta G_{binding}$ Hydrogen bonding	$\Delta G_{binding}$ Lipophilicity	$\Delta G_{binding}$ Van Der Waals
3w2r					
22	-138.987±19.71	-25.239±7.47	-1.77±0.34	-69.151±7.99	-75.04±5.77
902	-97.612±11.74	-28.717±15.57	-5.71±0.92	-37.687±3.93	-56.371±9.01
3nvy					
902	-72.583±13.58	-9.564±12.32	-1.90±0.32	-34.630±4.64	-45.556±7.89
890	-71.052±14.71	-9.973±6.48	-1.81±0.81	-34.740±6.19	-46.98±9.13

4. SUMMARY AND CONCLUSION

A large library of ligands was designed based on the curcumin scaffold. Various modifications were incorporated and a target search was carried out for these structures by screening through the critical targets involved in cancer. The BindingDB and SwissTarget were employed for this target screening. Later, the targets showing the highest potential recognized as EGFR2, and Xanthine oxidase were selected for molecular docking. Molecular docking of the library of curcumin derivatives revealed the top 2 best ligands against these targets namely ligands **22** and **902** against EGFR2 and **890** and **902** against xanthine oxidase. These hit molecules in complex with identified proteins were subjected to MD simulations for 100 ns. After evaluating all parameters, it was found that these hit molecules showed great potential to act as competitive inhibitors of EGFR2 and Xanthine oxidase. MM-GBSA studies revealed changes in binding free energies of these ligand-protein complexes, thereby further supporting the anti-cancer potential of these hit molecules. This study revealed ligands **22** and **902** as hits against EGFR2 and **890** and **902** against Xanthine oxidase respectively. Hence, all these hit molecules bear great potential as anti-cancer molecules.

Abbreviations

MD: Molecular Dynamics

RMSD: Root-mean square deviation

RMSF: Root-mean square fluctuation

rGyr: Radius of gyration

SASA: Solvent-accessible surface area

PSA: Polar surface area

MolSA: Molecular surface area

MM-GBSA: Molecular Mechanics Generalized Born Surface area

SSE: Secondary structural elements

Data and software availability

"The Data generated for the current work is available in the supplementary files"

REFERENCES

1. Opeyemi I, Paul Olamide O, Femi O, Olorunfemi Oyewole B, Olusola Olalekan E, Babatomiwa K, Abayomi Emmanuel A, Henry Nnaemeka O, Covenant Femi A, Ibukun Mary F, Aderonke Elizabeth F, Moses Orimoloye A, Sunday Amos O, Sergey S. Computer-aided drug design in anti-cancer drug discovery: What have we learnt and what is the way forward? Informatics in Medicine Unlocked., 2023; 41: 101332. https://doi.org/10.1016/j.imu.2023.101332
2. R. Kurczab, The evaluation of QM/MM-driven molecular docking combined with MM/GBSA calculations as a halogen-bond scoring strategy. Acta Cryst., 2017; B73: 188-194. https://doi.org/10.1107/S205252061700138X
3. Bilal S, Sajjad A, Jingyu L, Chanjin J, Dokyun Na. In silico methods and tools for drug discovery. Computers in Biology and Medicine., 2021; 137: 104851. https://doi.org/10.1016/j.compbiomed.2021.104851
4. Halgren TA, Murphy RB, Friesner RA, Beard HS, Frye LL, Pollard WT, Banks JL. Glide: a new approach for rapid, accurate docking and scoring. 2. Enrichment factors in database screening. J Med Chem., 2004; 47(7): 1750–9.
5. Hollingsworth SA, Dror RO. Molecular dynamics simulation for all. Neuron; 2018; 99(6): 1129–43.
6. Cui W, Aouidate A, Wang S, Yu Q, Li Y, Yuan S. Discovering anti-cancer drugs via computational methods. Front Pharmacol., 2020; 11: 733.
7. Ajaikumar B. Kunnumakkara, Preetha Anand, Bharat B. Aggarwal, Curcumin inhibits proliferation, invasion, angiogenesis, and metastasis of different cancers through interaction with multiple cell signaling proteins. Cancer Lett., 2008; 269: 199–225; Available from https://doi.org/10.1016/j.canlet.2008.03.009

8. R.A. Sharma, A.J. Gescher, W.P. Steward, Curcumin: The story so far. Eur. J. Cancer, 2005; 41: 1955-68; Available from https://doi.org/10.1016/j.ejca.2005.05.009
9. Schneider, C., Gordon, O. N., Edwards, R. L., & Luis, P. B. Degradation of Curcumin: From Mechanism to Biological Implications. J. Agric. Food Chem., 2015; 63(35): 7606–14. https://doi.org/10.1021/acs.jafc.5b00244
10. Lee, W.-H., Loo, C.-Y., Bebawy, M., Luk, F., Mason, R., & Rohanizadeh, R. Curcumin and its Derivatives: Their Application in Neuropharmacology and Neuroscience in the 21st Century. Curr. Pharamcol., 2013; 11(4): 338–78. https://doi.org/10.2174/1570159X11311040002
11. Malik, P., & Mukherjee, T. K. Structure-Function Elucidation of Antioxidative and Prooxidative Activities of the Polyphenolic Compound Curcumin. Chin. J. Biol., 2014; 1–8. https://doi.org/10.1155/2014/396708
12. Priyadarsini, K. The Chemistry of Curcumin: From Extraction to Therapeutic Agent. Molecules, 2014; 19(12): 20091–112. https://doi.org/10.3390/molecules191220091
13. Gordon, O. N., & Schneider, C. Vanillin and ferulic acid: not the major degradation products of curcumin. Trends Mol. Med., 2012; 18(7): 361–3. https://doi.org/10.1016/j.molmed.2012.04.011
14. Zhou, H., S. Beevers, C., & Huang, S. The Targets of Curcumin. Curr. Drug Targets, 2011; 12(3): 332–347. https://doi.org/10.2174/138945011794815356
15. Wilken, R., Veena, M. S., Wang, M. B., & Srivatsan, E. S. Curcumin: A review of anti-cancer properties and therapeutic activity in head and neck squamous cell carcinoma. Mol. Cancer, 2011; 10(1): 12. https://doi.org/10.1186/1476-4598-10-12
16. Islam, Md. R., Rauf, A., Akash, S., Trisha, S. I., Nasim, A. H., Akter, M., Dhar, P. S., Ogaly, H. A., Hemeg, H. A., Wilairatana, P., & Thiruvengadam, M. Targeted therapies of curcumin focus on its therapeutic benefits in cancers and human health: Molecular signaling pathway-based approaches and future perspectives. Biomed. Pharmacother., 2024; 170: 116034. https://doi.org/10.1016/j.biopha.2023.116034
17. Kunnumakkara, A. B., Anand, P., & Aggarwal, B. B. Curcumin inhibits the proliferation, invasion, angiogenesis and metastasis of different cancers through interaction with multiple cell signaling proteins. Cancer Lett., 2008; 269(2): 199–225. https://doi.org/10.1016/j.canlet.2008.03.009
18. Narsaiah Chelimela, Rajasekhar Reddy Alavala, Shobha Rani Satla. Curcumin – Bioavailability Enhancement by Prodrug Approach and Novel Formulations, Chem.

Biodiversity, 2024; 21(5): e202302030. Available from https://doi.org/10.1002/cbdv.202302030

19. Rajasekhar Reddy Alavala, P. Dinesh, A.S. Prabhakar, K. Umasankar, B. Shireesha, M. Bhagavan Raju. Mini Rev. Med. Chem., 2013; 13: 1769-77; Available from http://doi.org/10.2174/1389557511313120007
20. BindingDB database, https://www.bindingdb.org, UC San Diego.
21. Daina, A., Michielin, O., & Zoete, V. SwissTargetPrediction: updated data and new features for efficient prediction of protein targets of small molecules. Nucleic Acids Res., 2019; 47(W1): W357–W364. https://doi.org/10.1093/nar/gkz382
22. Sogabe, S., Kawakita, Y., Igaki, S., Iwata, H., Miki, H., Cary, D. R., Takagi, T., Takagi, S., Ohta, Y., & Ishikawa, T. Structure-Based Approach for the Discovery of Pyrrolo[3,2-*d*]pyrimidine-Based EGFR T790M/L858R Mutant Inhibitors. ACS Med. Chem. Lett., 2013; 4(2): 201–5. https://doi.org/10.1021/ml300327z
23. Cao, H., Pauff, J. M., & Hille, R. X-ray Crystal Structure of a Xanthine Oxidase Complex with the Flavonoid Inhibitor Quercetin. J. Nat. Prod., 2014; 77(7): 1693–99. https://doi.org/10.1021/np500320g
24. Joshi, N., & Alavala, R. R. Sulfonamido, amido heterocyclic adducts of tetrazole derivatives as BACE1 inhibitors: in silico exploration. Mol. Divers., 2024; 28(6): 4017–4049. https://doi.org/10.1007/s11030-023-10792-7
25. P., G., & M. K., K. Docking studies and molecular dynamics simulation of triazole benzene sulfonamide derivatives with human carbonic anhydrase IX inhibition activity. RSC Adv., 2021; 11(60): 38079–93. https://doi.org/10.1039/D1RA07377J
26. Genheden, S., & Ryde, U. The MM/PBSA and MM/GBSA methods to estimate ligand-binding affinities. Expert Opin. Drug Discov., 2015; 10(5): 449–61. https://doi.org/10.1517/17460441.2015.1032936
27. Al-Anazi, M., Khairuddean, M., O. Al-Najjar, B., Murwih Alidmat, M., Nur Syazni Nik Mohamed Kamal, N., & Muhamad, M. Synthesis, anticancer activity and docking studies of pyrazoline and pyrimidine derivatives as potential epidermal growth factor receptor (EGFR) inhibitors. Arab. J. Chem., 2022; 15(7): 103864. https://doi.org/10.1016/j.arabjc.2022.103864
28. Wang, S., Xu, X., Pan, C., Guo, Q., Li, Q., Wan, S., Li, Z., Zhang, J., & Wu, X. Identification of New EGFR Inhibitors by Structure-Based Virtual Screening and Biological Evaluation. Int. J. Mol. Sci., 2024; 25(3): 1887. https://doi.org/10.3390/ijms25031887

29. Ghallab, D. S., Shawky, E., Metwally, A. M., Celik, I., Ibrahim, R. S., & Mohyeldin, M. M. Integrated in silico–in vitro strategy for the discovery of potential xanthine oxidase inhibitors from Egyptian propolis and their synergistic effect with allopurinol and febuxostat. RSC Adv., 2022; 12(5): 2843–72. https://doi.org/10.1039/D1RA08011C
30. Fatima, I., Zafar, H., Khan, K. M., Saad, S. M., Javaid, S., Perveen, S., & Choudhary, M. I. Synthesis, molecular docking and xanthine oxidase inhibitory activity of 5-aryl-1H-tetrazoles. Bioorg. Chem., 2018; 79: 201–11. https://doi.org/10.1016/j.bioorg.2018.04.021
31. Vitale, R. M., Antenucci, L., Gavagnin, M., Raimo, G., & Amodeo, P. Structure–activity relationships of fraxamoside as an unusual xanthine oxidase inhibitor. J. Enzyme Inhib. Med. Chem., 2017; 32(1): 345–54. https://doi.org/10.1080/14756366.2016.1252758